Energy materials

Bioinspired oxygen selective membrane for Zn–air batteries

Olga Krichevski[1], Ramesh Kumar Singh[1], Edward Bormashenko[2], Yelena Bormashenko[2], Victor Multanen[2], and Alex Schechter[1,*] (iD)

[1] Department of Chemical Sciences, Ariel University, Ariel 40700, Israel
[2] Engineering Faculty, Chemical Engineering, Biotechnology and Materials Department, Ariel University, Ariel 40700, Israel

ABSTRACT

Zn–air and other metal–air batteries suffer from limited shelf life due to carbonization by CO_2 and evaporation of water through the cathode. Bioinspired oxygen selective membranes (OSMs) with common similarities to lungs alveoli were prepared and applied as an oxygen selective passive membrane on the cathode of the Zn–air batteries, which limit CO_2 and H_2O transport while actively supporting O_2 flux. The OSMs were prepared from polycarbonate and iron(II) phthalocyanine in volatile chlorogenic solvent ("breath figures self-assembly" mechanism) under controlled humidity conditions. Membranes were characterized by scanning electron microscopy, UV–visible spectroscopy, and gas chromatography. These membranes contain polycarbonate in a pulmonary alveolus-like structure of 0.2–4.0 microns thick, inclosing iron(II) phthalocyanine as an oxygen carrier molecule. The electrochemical measurements are performed to evaluate the membrane O_2 permeability in both half- and full-cell Zn–air configurations. The effect of relative humidity, iron(II) phthalocyanine, and polycarbonate content is investigated during the optimization of membrane permeabilities and selectivity results. By installing the OSM on top of the cathode of a Zn–air prototype cell, we were able to reduce the water evaporation by 88% while supporting an oxygen limiting current of 73 mA cm^{-2}_{OSM} with an OSM (PC 11%, FePc 9.1%).

Handling Editor: Mark Bissett.

Address correspondence to E-mail: salex@ariel.ac.il

GRAPHICAL ABSTRACT

In this contribution, we present an oxygen selective membrane (OSM) to increase the shelf life of the Zn–air cell. By applying OSM on top of the Zn–air cell cathode, we successfully demonstrated the reduction in the water evaporation by 88% while supporting an oxygen limiting current of 73 mA cm$^{-2}_{OSM}$.
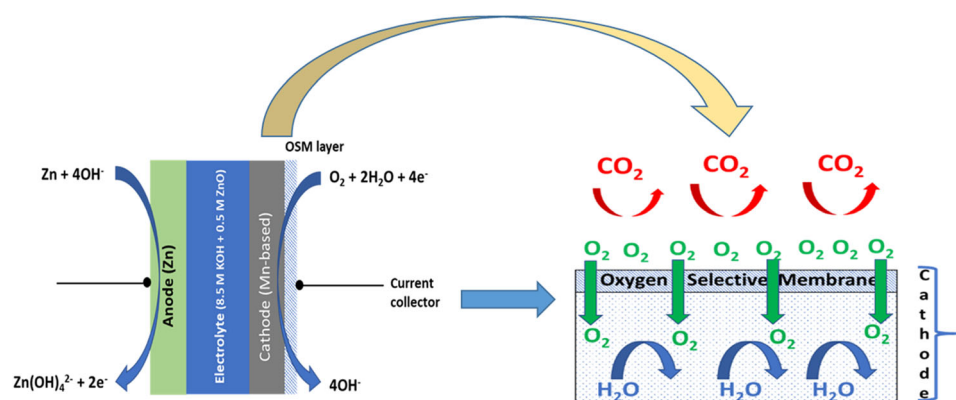
Introduction

Metal–air batteries [1, 2] are electrochemical energy storage devices with high energy density comprised of an active metal anode and an oxygen cathode. Primary Zn–air battery is the most mature metal–air technology, which has already been commercialized, while aluminum–air [3], magnesium–air [4], sodium–air [5], and lithium–air [2, 6] have more specific narrow application segment. In the past decade, intensive research efforts have been devoted to the development of rechargeable metal–air batteries [7–12]. Oxygen cathode plays a vital role in the field of Zn–air batteries [13, 14]. Pan et al. critically reviewed the transition metal oxides (TMOs) as a bifunctional catalyst for Li–air and Zn–air batteries, highlighting the challenges for developing advanced bifunctional catalysts based on TMOs for rechargeable Li–air and Zn-batteries [15]. Among the most challenging shortcoming of these devices is the limited control over oxygen flux into the cell from the air electrode as they affect oxygen purity and the solvent evaporation through the same cathode. All these limitations shorten the life of primary batteries and may hamper future rechargeable metal–air battery cycle life.

One approach is to apply oxygen selective membranes (OSMs) on the cathode side of the Zn–air cell, which selectively transfers oxygen from the air while blocking the CO_2 and water transport from the cell, respectively. OSMs comprise a carrier molecule that selectively and reversibly binds molecular oxygen (similar to the iron site in the hemoglobin), thus having the potential of increasing the rate of oxygen transport relative to other gases. Due to the smaller water kinetic diameter (2.60 Å) compared to that of oxygen (3.46 Å) [16, 17], porous membranes optimized for high O_2 permeability may hardly prevent water transport from the electrolyte of a cathode covered by an OSM. On the other hand, the rate of carbon dioxide transport through most OSM is often comparable to O_2, where the selectivity ratio of P_{O_2}/P_{CO_2} is often less than unity [18, 19]. One of the means of enhancing O_2 permeability is by reducing the membrane thickness. However, by doing so, it decreases its mechanical strength and susceptibility to pinhole failure.

Several reports describe incorporating organometallic compounds into the polymeric structure of the membrane, particularly cobalt-based

molecules, which was claimed to increase the selectivity of oxygen over nitrogen by more than one order of magnitude [20–22]. Moreover, the metal-phthalocyanine (CoPc and FePc) [23] and its derivatives exhibit impressive oxygen reduction catalytic activity [24], electronic properties [25], and chemical or thermal stability [26]. These CoPc-based membrane has been reported to provide relatively high O_2 permeability at low-pressure drops and consistent flow rates in applications such as pre-filtration and gas separation [22, 27]. Preethi et al. have reported membranes with CoPc as an O_2 carrier molecule in the copolymer of vinyl imidazole and octyl methacrylate [20]. The permeability coefficient of oxygen (P_{O_2}) through a membrane of this class was reported to be much higher ($P_{O_2}/P_{N_2} > $ 20) than that of N_2 gas, and therefore, it was offered as a possible O_2 filtration from air [20]. Nishide et al. have reported a poly(vinylidene dichloride)-cobalt porphyrin membrane with highly selective oxygen permeation, providing support for hopping transport of O_2 via fixed cobalt porphyrin carrier [28]. In all the reported studies, the membrane containing oxygen carrier molecules had no control over their structure and porosity to improve their gas permeabilities.

In work, we applied a passive OSM on the Zn–air cell cathode to enable the control of gases in and out of the electrochemical cell. The OSMs were prepared by using polyolefin incorporating iron(II) phthalocyanine (FePc) by a "breath-figure" (BF) self-assembly method, which provided reasonable control over the basic pore structure and shape. FePc has several advantages over CoPc: (i) It is less expensive and (ii) less harmful and (iii) Fe also considered as critical raw material-free element. The resulting OSMs have a porous structure with a submicron separating skin, loaded with FePc oxygen carrier, which tries to mimic the lungs' alveoli. Several fabrication parameters affecting the OSM properties, namely the relative environmental humidity, FePc and polycarbonate contents, were investigated during the OSM optimization. Finally, the O_2 permeability and water retention rates are estimated on a selected OSM using a Zn–air battery proving the concept of passive OSM protecting layer.

Experimental section

Materials

Polycarbonate (molecular weight (MW) 56,000) from Bayer, poly(bisphenol a carbonate) (MW 34,000) from Sigma-Aldrich, dichloromethane AR-b (Biolab Ltd), chloroform AR-b (Biolab Ltd), acetone AR-b (Biolab Ltd), ethanol AR-b (Biolab Ltd), iron (II) phthalocyanine 95% (Fe(II)Pc) (Strem chem.), stainless steel mesh (SS) (500 μm), and Gen-3 zinc–air cells from "Electric Fuel" company were used.

Instrumentation

The membranes were characterized by using SEM (JEOL JSM-6510LV) and ultra-high-resolution Maia 3 FE-SEM (TESCAN) for the image in Fig. 6a, and Figs. 2, 3, and S2 were recoded using JEOL JSM-6510LV. UV–visible spectroscopic measurements were performed using a Cary® 50 Bio UV–visible spectrophotometer (Varian Medical Systems, USA). DC electronic load (Chroma 63,102) was applied for limiting current measurements from the Zn–air battery. Gas chromatography was performed using a YL6100 GC (Young Lin Instrument Co. Ltd., Korea). For gas chromatography experiments, the flame ionization detector (FID) and thermal conductivity detector (TCD) were used. The carrier gas is argon with flow 100 ml min^{-1}. The Biologic VSP 300 work station was used for the "half-cell" measurement.

Membrane preparation

The membranes were prepared using a dip coating method, as described by Bormashenko et al. [29] and other groups [30]. Membranes were prepared on two kinds of substrates (i) polypropylene (PP) and (ii) stainless steel (SS) metal mesh with different apertures. In short, a 5 cm × 5 cm stainless steel mesh support was first immersed in the polymer solution. Polycarbonate (PC) solutions of Fe(II) phthalocyanine (FePc) were prepared by dissolving PC and FePc, at selected weight percent, in a dichloromethane and chloroform solvent (volumetric ratio of 9:1). The volumetric ratio of the given solvents was determined in our previous studies [31]. The detailed calculation of PC and FePc weight percentage is given in the supporting information. Fabrication of OSMs by the dip-coating method includes a substrate

immersion stem in a dissolved polymer solution bath for 6 s and removal from the bath at a constant rate of 42 cm min^{-1}. After drying in air at 298 K at 55–60% relative humidity (RH), the membranes were peeled from the PP film for inspections. The humidity exerts a crucial impact on the breath figures self-assembly; [30] thus, the special chamber enabling precise control of the humidity with an accuracy of ± 1% RH was used. After initial optimization on the PP substrate, the next samples were prepared on SS mesh with higher PC concentration to obtain mechanically stable membranes.

Selectivity measurements

The amount of FePc in the membranes was verified by UV–visible measurement. The calibration curve was generated from the solution of PC and FePc and the amount of FePc in the membrane sample was confirmed, which is in line with the nominal composition of FePc (Fig. S1 and Table S1). Oxygen and CO_2 permeability measurements were performed using gas chromatography under a constant flow of air/N_2 on a 1 cm^2 free-standing membrane (PC 5 wt% and 5 wt% of FePc). The permeability (cm^3 cm^{-2} min^{-1}) of O_2 and CO_2 in the inert gas was calculated by integrating the GC peak signals using Eqs. (1 and 2) given below.

$$O_2 \text{ permeability } (P_{O_2}) = \{[S_{O_2} \times C_{O_2}]/S_{air}\} \times F \quad (1)$$

$$CO_2 \text{ permeability } (P_{CO_2}) = \{[S_{CO_2} \times C_{CO_2}]/S_{air}\} \times F \quad (2)$$

where S_{O_2} is the peak area of oxygen, S_{CO_2} is the peak area of CO_2, C_{O_2} is the concentration of O_2 in air, C_{CO_2} is the concentration of CO_2 in air, S_{air} is the peak area of oxygen in the air, and F is the flow rate of inert gas (100 cm^3 min^{-1}).

The selectivity (P_{O_2}/P_{CO_2}) of OSMs was calculated from the O_2 and CO_2 permeability measurements from GC.

Electrochemical measurements

Initial optimization of O_2 limiting current (I_{lim}) was evaluated in a Zn–air half-cell filled with 8.5 M KOH electrolyte. A Ni mesh was used as a counter electrode, Zn wire as a reference electrode, and the air electrode comprised of Mn-based catalysts was used as a working electrode (prepared by "Electric Fuel" company). The I_{lim} was calculated by recording linear sweep voltammograms (LSVs) from 1.3 to 0.8 V at a scan rate of 2 mV s^{-1}. The water transport measurements were performed using a stainless steel vessel containing 1 ml of 8.5 M KOH solution and housing a 7-cm^2 membrane on top. Teflon and cathode layers were placed in control experiments.

For the full cell measurements, Gen-3 Zn–air batteries with MnO_2-based cathode (Fig. 1a) from "Electric Fuel Company" (Epsilor-*Electric Fuel, Ltd, Israel*) were used for determining oxygen limiting transport current and relative reduction in water transport (RRWT) through OSMs covering the cathode. Mesh-supported membranes were assembled on the Zn–air by attaching with scotch tape to the cathode as a passive component (Fig. 1b). Oxygen reduction limiting current was measured from the discharge curve by using load currents from 0 to 1.5 A with an increasing current step protocol of 30 mA and 2 min. A distinct point marked on the discharge curve for the limiting current, which represents the current at which the oxygen supply through the membrane becomes a limiting parameter, and the slope of the IV curve becomes more negative after this point. However, the Zn–air battery without OSM shows no limitation of O_2 transport in the selected current range. Beyond this point, the discharge curve slope becomes steep in the cell covered by OSM due to mass transport through the OSM, which leads to oxygen depletion at the cathode (Fig. 1c).

Thus, the O_2 transport in mA cm^{-2}$_{OSM}$ of OSM was calculated or converted to oxygen permeability cm^3 cm^{-2} min^{-1} by applying Eq. 3.

$$P_{O_2} = I_{lim} \times V/(4 \times F \times 60) \quad (3)$$

where P_{O_2} is the oxygen permeability (cm^3 cm^{-2}-min^{-1}), I_{lim} is the oxygen limiting current (mA cm^{-2}), V is the standard molar volume at 25 °C (24,780 cm^3 mole^{-1}), and F is the Faraday constant (26.801 Ah mole^{-1}).

The RRWT measurement was performed by placing the battery in the environmental chamber (37 °C and 17% RH) before and after the membrane installation, similar to the stainless steel container testing. We have maintained the constant humidity during the water evaporation measurement and the synthesis, not during the electrochemical measurement, which typically were shorter. The RRWT was measured by the mass change of Zn–air batteries with time, due to water evaporation from the cathode protected by OSM and without this membrane as a

Figure 1 Zn–air battery reference (**a**) and OSM assembled on Zn–air battery cathode (**b**). Discharge curves of Zn–air battery with and without OSM (**c**).
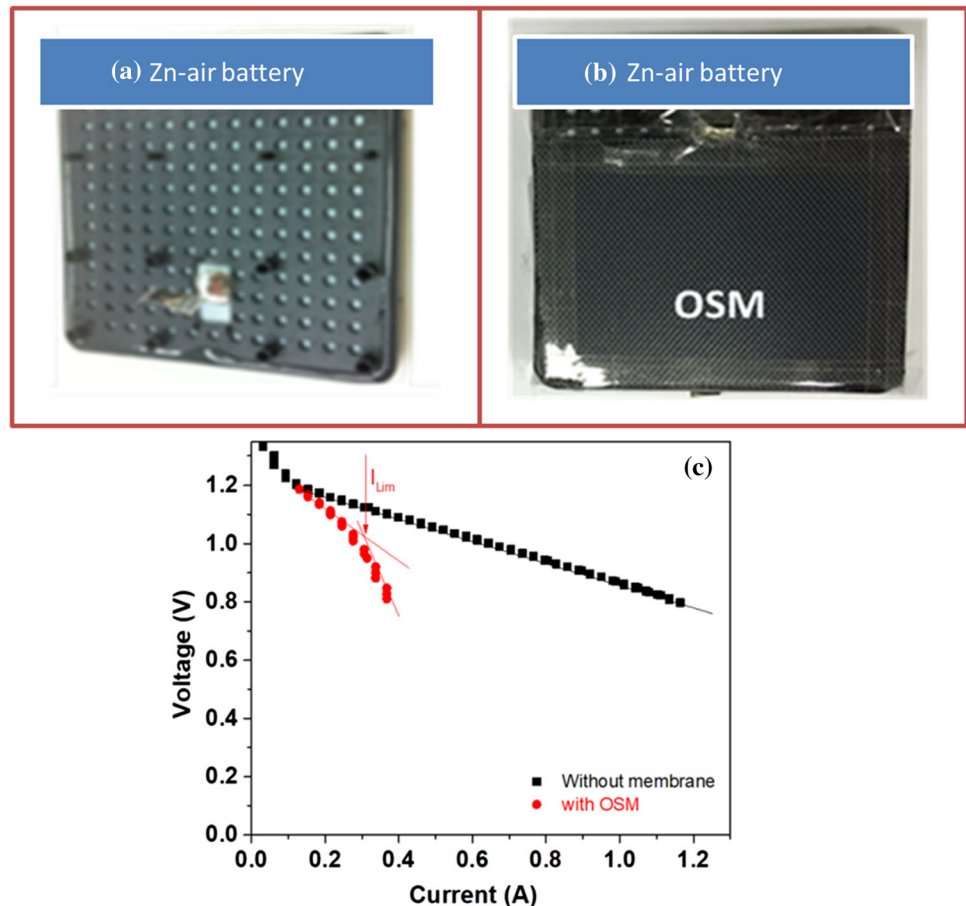
reference, under the same controlled temperature and humidity conditions. An essential parameter in this respect is the percentage of reduction in water transport through the OSM compared to a reference cell on a regular Zn–air battery (Eq. 4).

$$\% \ RRWT = \left(1 - \frac{\Delta m_{\text{mem.}}}{\Delta m_{\text{ref.}}}\right) \times 100 \qquad (4)$$

where $\Delta m_{\text{mem.}}$ is the weight loss of membrane (g cm^{-2}), $\Delta m_{\text{ref.}}$ is the weight loss from the reference cell (g cm^{-2}), and RRWT is the relative reduction in water transport.

The water permeability was calculated using Eq. (5) from the Zn–air battery at 37 °C.

$$P_{H_2O} = \frac{\Delta m}{M \times V} \qquad (5)$$

where P_{H_2O} is the water permeability (cm^3 cm^{-2} min^{-1}), Δm is the water loss in g cm^{-2} min^{-1}, M is the molar mass of water (18 g mole^{-1}), and V is the molar volume at 37 °C (25,430 cm^3 mole^{-1}). The selectivity (P_{O_2}/P_{H_2O}) of OSMs was calculated from the O$_2$ and H$_2$O permeability measurements from Zn–air cells.

Results and discussion

Initial optimization of membrane on polypropylene substrate

Membranes with various polycarbonate concentrations were prepared on polypropylene (PP) substrate and studied using scanning electron microscopy (SEM). Figure 2 shows the SEM images of membranes made from 0.5 to 5 wt% PC solutions on the PP substrate. The membranes in Fig. 2 are formed on a flat PP surface with a porous structure that is only on one side (facing the air), while the opposite side (facing the PP) is highly dense. Therefore, the membranes required low PC content (0–5 wt%) to maintain mechanical stability. The porosity formation of "breath figure (BF)" surface polymers is a well-established research area in the literature [32]. Figure 2 shows spherical shape pores formed on the outer surface of the polysulfone membranes film. The limited diameter of these pores varies between 1 and 15 μm, which inadequate for BET analysis. Size

Figure 2 SEM images of "upper side" view of membranes films prepared from solution of **a** 0.5%, **b** 1.5%, **c** 2%, **d** 3% and **e** 5 wt% of PC (56,000 MW) prepared on the polypropylene film as a supporting substrate. The scale bar 5 μm in all images (**b-e**). Due to space constraints, the "bottom side" images of these samples are shown in Figure S2, respectively.
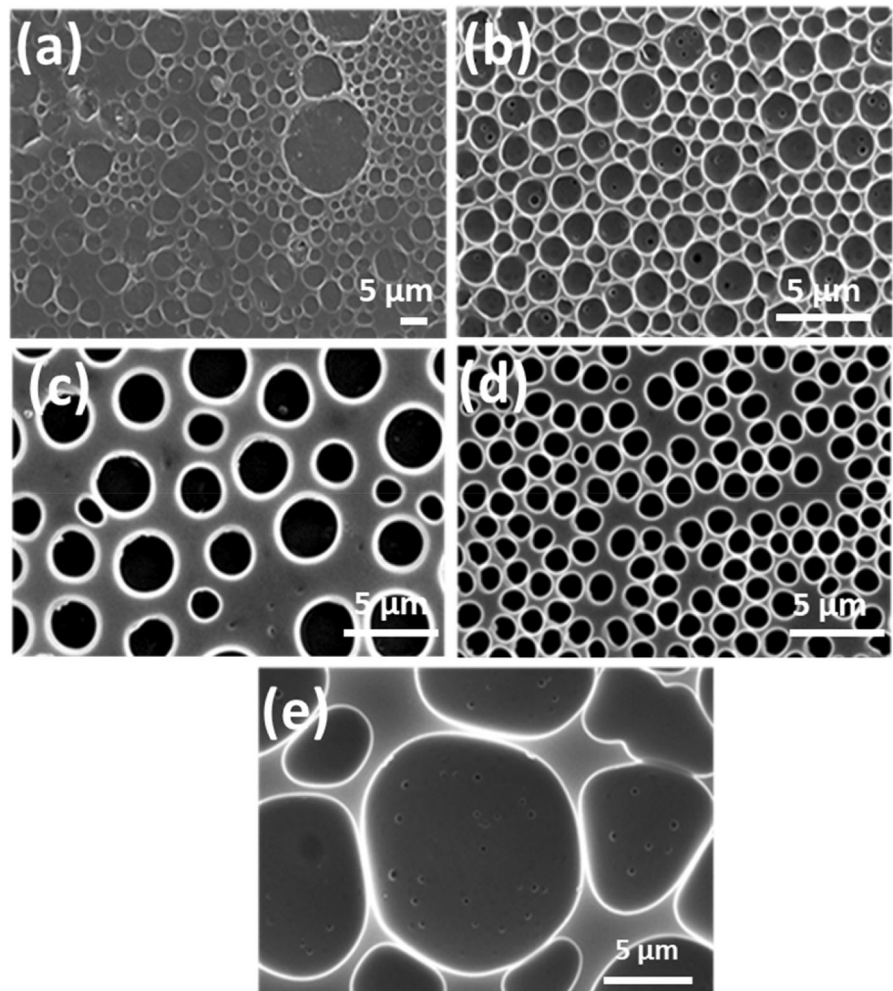
distribution can be controlled by controlling the formation conditions (humidity, solvents, concentration, and lifting speed of the sample from the solution). An inspection of the pores was done based on the SEM image.

An image of a typical free-standing film attained after peeling the membrane from the substrate displays two different structures on each side. The "upper side" of the film, which was exposed to the humid air atmosphere exhibit typical "BF-pattern," is depicted in Fig. 2, and the "bottom side" of the membranes which were in contact with the PP substrate displays a dense "skin-like" structure (Fig. S2). Further details about the pore evolution and BF patterns can be found in our previous articles [27, 29]. Very generally, "BF" self-assembly occurs when the thin layer of a polymer solution rapidly dried in a humid atmosphere. Rapid evaporation of the low boiling point solvent cools the air–polymer interface. Subsequently, intensive condensation of small water

droplets occurs on the liquid polymeric layer [33]. The water droplets then sink into the solution, eventually forming a closely packed, highly uniformly distributed, honeycomb pattern upon complete evaporation of the selected solvents [27, 29, 33]. The simplicity of the BF technique allows the preparation of ordered porous reliefs by using a wide variety of polymers and different macromolecular architectures (linear, star, graft, dendritic, hyper-branched polymers, and coil–coil or rod-coil diblock copolymers) during the last years [17, 30, 34–38].

Figure 2a shows the "upper side" of a membrane prepared from a 0.5 wt% polycarbonate polymer solution. The membrane was too thin and brittle and could not be removed from the PP substrate; therefore, the corresponding smooth "bottom side" is not shown in the SEM images. This membrane was imperfect, having thick regions constituting a link and node structure delineating an open non-uniform perforation that passes through the membrane.

Figure 2b shows the upper side of the membrane made from a polymer solution containing 1.5 wt% PC with a high density of holes (45×10^6 holes per cm^2). The density of the holes is obtained by counting the holes in a given area. The bottom side view of this film presents a markedly, more significant number of defects (94×10^6 defects per cm^2). These defects are smaller perforations located at the lowermost parts of the larger holes that can pass through the thinner sunken regions of the membrane (Fig. S2(b_1)). It assumed that the defects formed during the detachment of the film from the PP substrate. The thickness of the membrane is prepared on a flat surface is in the range of 0.5–4 μm, and it is well controlled. However, the membrane prepared on a metal grid is less uniform.

BF self-assembly yielded a uniform distribution of holes; however, defect density is too high for selective OSMs. For further explanation on "BF" formation, please refer to the book by Rodríguez-Hernández [32]. Therefore, the PC concentration was increased to reduce the number of defects perforating the "bottom side" of the membrane. Figure 2c shows SEM images of the "upper side" of the membrane made from a 2 wt% PC solution, which exhibits ∼ 7.5 times lower density of holes (6.0×10^6 holes per cm^2) compared to a membrane prepared from 1.5 wt% PC solution, which has an average hole size of 2.6 μm and 72 times lower defects (1.3×10^6 defects per cm^2) as seen on the bottom side (Fig. S2(c_1)). Upon the increase in PC concentration to 3%, the density of holes (37.0×10^6 holes per cm^2) grew compared to membranes prepared from 2% PC, the average hole size was 1.5 μm (Fig. 2d), and relatively lower defect density of 0.5×10^6 defect per cm^2 was detected (Fig. S2(d_1)), which is ∼ 2.5 lower compared to the 2 wt% prepared membrane. With a further increase in PC concentration to 5 wt%, the hole density decreased significantly to 2.0×10^6 holes per cm^2, because of an increase in the average hole size to ∼ 8 μm as seen from Fig. 2e. Similar to the results obtained with 3 wt% PC solution, when viewed from the bottom side, it was established that there are more defects (26×10^6 defects per cm^2) than with the 3% polymer solution (Fig. S2(e_1)). Based on these results, it is concluded that there is an optimum PC in membranes prepared with 3 wt% PC concentration on PP substrate, exhibiting a relatively higher density

of holes (37×10^6 holes per cm^2) with the lowest defect density and it also provides good mechanical stability. It is agreed that an increase in the concentration of the polymer is expected to result in a decrease in the pore size. This can be explained by the increased capacity of the polymer to stabilize the larger surface area of the water droplets before the precipitation of the polymer around the water droplet [38]. Nevertheless, these preliminary results of membranes prepared on PP suggest that further optimization of the substrate and forming solution concentration was still required. Hence, a stainless steel (SS) mesh was examined as an air open support which provides: (i) better dispersion of holes on both sides of the film, (ii) reduce the contact surface between the film and the support in the substrate, which is believed to be the cause of the defects and provide better mechanical stability and ease of handling.

Membranes prepared on stainless steel mesh

Breathfigure method creates a porous layer over a dense layer when fabricated on PP substrate or any smooth surface. Here, we aimed to form breath figure pores on both sides of the membrane; therefore, SS mesh was applied to support the process on both sides of the curing membrane. Membranes without FePc or with low content (less than 5% FePc) have significantly lower permeability values. Implementation of this understanding led to incorporating SS mesh to support the polymeric structure by replacing the continuous substrate of PP with a mesh of different hole sizes. In this study, SS non-woven meshes with a rectangular hole shape and length size of 500 microns were applied. Figure 3a shows the SEM image of a membrane prepared from 11% PC and 9.1% FePc solution supported on this mesh. Inset to Fig. 3a shows the bare SS mesh. Generally, the high permeation rate of ideal gases was dictated by the shortest diffusion length. However, as shown above, very thin membranes with breath figure structures below prepared from dilute PC solution are unstable. A magnified view of cross-section SEM images of the same membrane is shown in Fig. 3b and c. The high concentration of 11 wt% PC in this experiment was applied to improve the uniform coating over the SS

Figure 3 SEM image of **a** SS mesh with the membrane (PC (56,000 MW) 11% wt. and FePc 9.1 wt%), **b** a cross-section of the membrane close to SS mesh, and **c** an image of the membrane taken for the center of the open hole of SS mesh as shown by the guiding arrows extended from **a**. The inset to **a** shows the SS mesh.
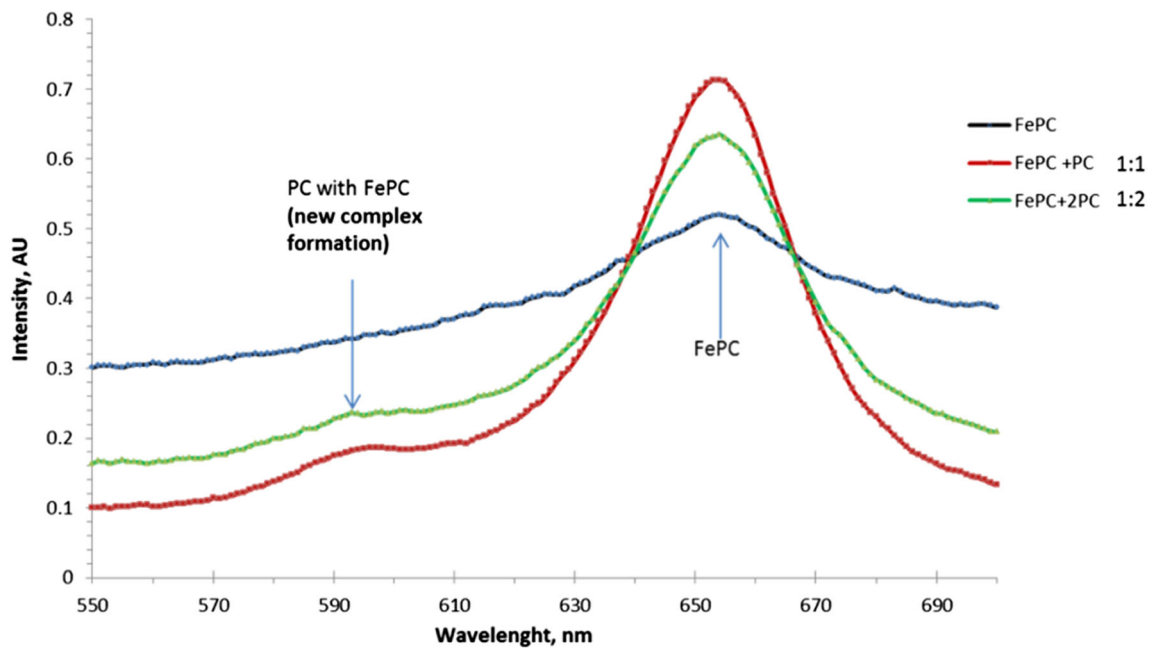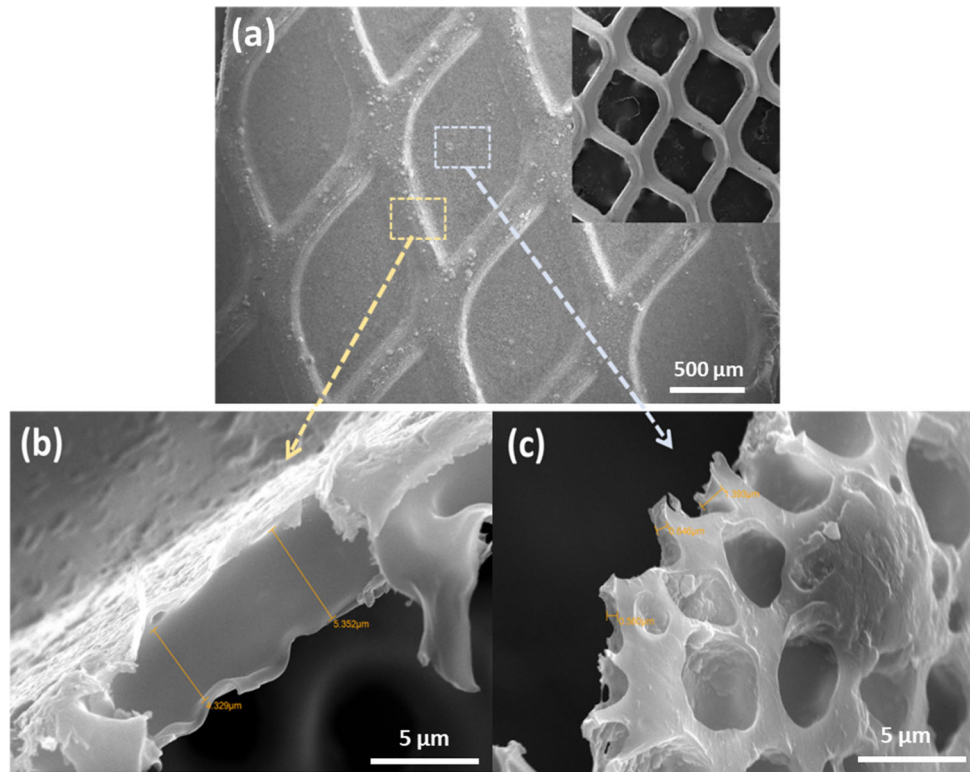
Figure 4 UV–visible spectra of chloroform and dichloromethane solutions: blue line FePc, FePc: PC 1:1 wt (red), and FePc: PC 1:2 (green).

mesh and reduce defects. The thickness of this polymer layer at the vicinity of the thread is about 5 µm (Fig. 3b) and 0.1–0.3 µm (Fig. 3c) in the thinner center region of the grid holes of the mesh. It is important to emphasize that the BF pores are formed on both sides of the membrane, exposed to air, and

not on one side, as seen in the membrane prepared on PP film. By increasing the FePc concentration in the polymer, precise adjustments to the deep coating bath had to be applied to improve the dissolution of the phthalocyanine molecules.

The formed solution of FePc, which is a well-known chromophore, was inspected spectroscopically. The UV–visible spectra of FePc and FePc in solution with PC at a given ratio in 1:1 and 1:2 FePc:PC are shown in Fig. 4. A new peak at 595 nm was observed in solutions containing PC and FePc. This peak is assigned to the interaction or complex formation between the carbonate groups in the polymer and the dissolved iron phthalocyanine molecules in the solvent mixture. Oxygen carrier molecule (FePc) reversibly coordinates to the slightly negatively charged oxygen of the carbonate and thereby facilitate high solubility or dispersion of FePc in the solution as indicated by the more intense peak at 655 nm of solutions containing PC and FePc compared to FePc solution with the same FePc concentration. The dispersion and interaction of the polymer with FePc are an essential parameter in oxygen transport through OSM. Therefore, the higher concentration of PC was used to further improve the dissolution and dispersion of FePc in the polymeric matrix via complex formation.
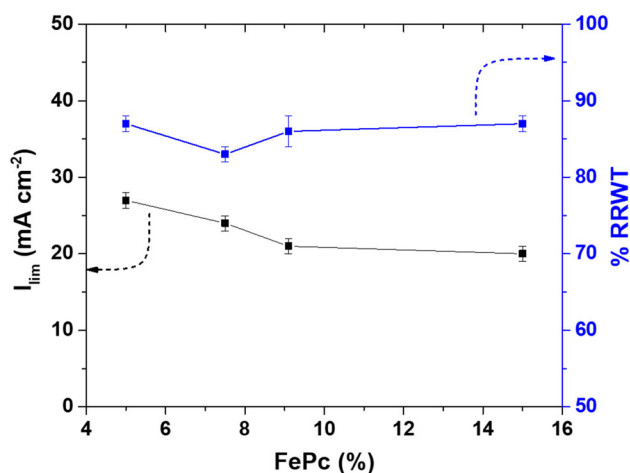
Figure 5 O_2 limiting current and relative reduction in water transport (RRWT) as a function of FePc content in the membrane (PC 11 wt%). The error bar is taken from three experimental repeats.

Optimization of relative humidity and FePc concentration

Effect of FePc concentration

The effect of FePc content in the OSM on oxygen permeability and RRWT was examined by varying its composition of FePc from 5 to 15 wt% in the bath solutions containing a fixed PC concentration of 11 wt% PC in dichloromethane: chloroform 9:1. These samples were mounted on the air-exposed cathode of Zn–air batteries, and the limiting current (I_{lim}) resulting in O_2 transport through the membrane was determined from the I-V discharge curves (Fig. 5). Moreover, FePc is known to have oxygen-binding capabilities. As shown in the UV results, there is an interaction between the polycarbonate and the oxygen carrier (FePc). A slight decrease in I_{lim} from 25 mA cm^{-2} at 5% to 18 mA cm^{-2} at 9 wt% FePc changes very little at a higher concentration of 15% wt. Conversely, the RRWT does not change significantly with FePc content and remains at 86–88% throughout the entire composition range. Below 5 wt% FePc, O_2 limiting current is very low (during our initial optimization), and above 15 wt% the FePc tends to precipitates, which lowers the homogeneity of the forming solution and resulting fabricated OSMs. Below 5 wt%, the concentration is too low to facilitate effective oxygen transport between FePc binding sites or by diffusion, while at higher concentrations than 5 wt%, the formation of small solid FePc particles in the membrane has been observed, thus hampering the diffusivity and decreasing the O_2 limiting current. We experimented with a bare PC membrane (without FePc), which exhibited three times lower O_2 permeability than PC-FePc samples. This is an expected observation since these membranes do not support facilitated oxygen transport by FePc, which is known to have O_2-binding property and serves as an oxygen reduction catalyst. Based on these results, OSM with 5 wt% FePc concentration is used for further optimization.

Effect of relative humidity in air on OSM structure and permeability

SEM images of OSMs with PC 15% and 5% FePc prepared under air controlled relative humidity of 45–60% are shown in Fig. 6a. Below 45%, the formation of breath figure assembly is not sufficient, and it

(a)

(b)
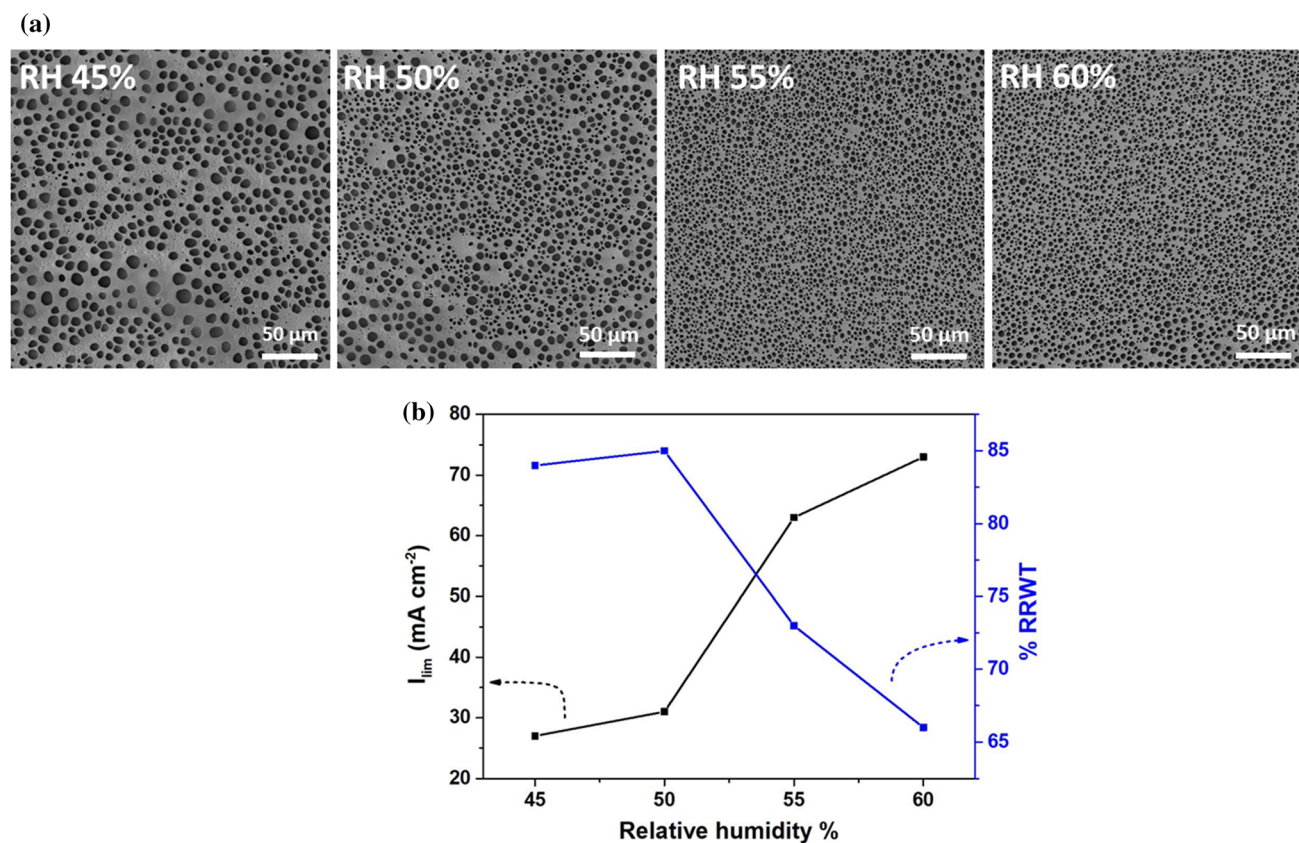
Figure 6 SEM images of OSMs (PC 15% and FePc 5%) prepared under relative humidity air atmosphere (**a**) and corresponding O_2 limiting current and RRWT (**b**). The SEM scale bars in all the images (**a**) is 50 μm.

Table 1 Average pore size in OSM consisting of PC (MW 56,000) 15 wt%, FePc 5 wt.%, prepared under selected relative humidity (RH) conditions

RH%	Pore size (μm)
45	10 ± 2
50	6 ± 1
55	4 ± 1
60	3 ± 1

was challenging to maintain constant humidity above 60% in large volume used as the environmental chamber in this study. The pore size diameter seen in Fig. 6a decreases from 10 to 3 μm (Table 1) at the corresponding increase in RH from 45 to 60%, which is explained by the formation of denser water droplets coverage at higher humidity. Measurements of O_2 limiting currents and RRWT are shown in Fig. 6b. The O_2 limiting current increases, and the RRWT decreases with RH in line with the decrease in pore size of the membrane (Fig. 6b). Namely, at high RH, the pores are smaller, which provides a larger contact area of the OSM, leading to higher O_2 adsorption surface and transport, but at the same time, the water

evaporation rate also decreased for the same reason. An optimum result is observed at 55% RH, corresponding to the pore size of the diameter of 4 μm. Interestingly, the O_2 limiting currents and RRWT of OSMs prepared from lower average MW of 34,000 PC under controlled RH exhibit almost no change with RH (Fig. S3). We ascribe this observation to segmental cooperative O_2 transport assisted by the lower PC molecular weight, which could provide shorter O_2 hopping distance between FePc sites [22, 28].

Gas chromatography selectivity measurements

Gas permeation properties through the membrane were investigated by gas chromatography (GC) connected to the fuel cell hardware used as the membrane fixture (Fig. S4). For these measurements, the 1 cm^2 free-standing OSM (PC 5% and FePc 5%) was placed between two graphite plates with gas flow channels; airflow of 100 ml min^{-1} was supplied in one side of the membrane ($P < 1$ psi), and
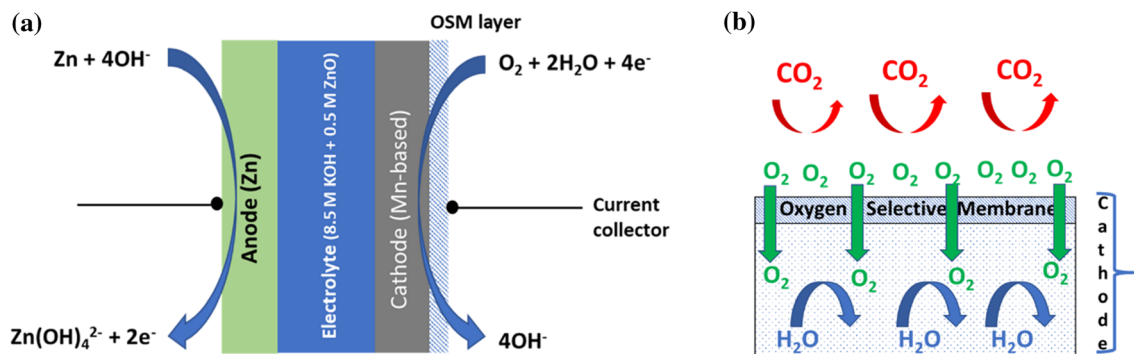
Fig. 7 Scheme of Zn–air cell (**a**) and magnified view of the cathode with oxygen selective membrane (**b**); the scale is not in line with the thickness of layers.

100 ml min^{-1} of helium gas on the other side was connected to the GC automatic sampling valve. The peaks of oxygen, nitrogen, and carbon dioxide in the sampled helium stream were analyzed with respect to pure gas standards and the dry air. Measured OSM had nitrogen/oxygen selectivity (P_{N_2}/P_{O_2}) of 2.68 and oxygen/carbon dioxide (P_{O_2}/P_{CO_2}) of 1083. The values were compared with plain Teflon filter (no selectivity) under the same flow, pressure, and temperature conditions, which yielded P_{N_2}/P_{O_2}= 3.95 and P_{O_2}/P_{CO_2} = 550. These selectivity values are 1.47 and 1.97 times higher, respectively, supporting the OSM's active oxygen facilitated mechanism. In CO_2 measurements, we compare the peaks of CO_2 (400 ppm) by analyzing the air without the membrane and the O_2 permeation peak with the membrane installed. The ratio of these peaks provides the CO_2 permeation rate. We assume that such a small concentration of 400 ppm CO_2 does not alter the membrane properties, in support of 2 fold increase in the P_{O_2}/P_{CO_2} selectivity measured with the membrane.

Permeability measurements from the Zn–air battery

Finally, the measured permeation rates values of O_2 and % RRWT were calculated through OSM prepared on SS mesh of size 500 μm using PC (11 wt%) and FePc (9.1 wt%) installed on Zn–air battery. Polycarbonate and the membranes exposed to 8 M KOH solutions for 6 h with no noticeable effect on the mechanical, chemical, or permeability properties. The maximum RRWT and O_2 limiting current of our OSM are 88% and 73 mA cm$^{-2}_{OSM}$, respectively, which is close to that measured from half-cell observed. The calculated OSMs selectivity ($P_{O_2}/$

P_{H_2O}) is in the range of ∼10-15 or higher. The reported selectivity (P_{O_2}/P_{H_2O}) in oxygen selective membranes for Li–air batteries is 2.5–5 [18]; however, our membrane for the Zn–air cell is significantly higher. The measured O_2 permeability is 1.28×10^{-9} mol m^{-2} s^{-1} pa^{-1} compared with 9.59×10^{-8} mol m^{-2} s^{-1} pa^{-1} (74 mA cm^{-2} from Fig. 6), which is 80 times higher than the reported value [39].

In summary, the concept of the OSM for the Zn–air battery is shown in Fig. 7. Figure 7a displays a Zn–air cell scheme, and Fig. 7b illustrates the functionalities of an OSM installed over the cell cathode, which allows selective O_2 permeation, blocking of CO_2, and preventing water evaporation from the cell. The OSM is covering the cathode side just 2–4 mm above the cathode material itself, properly sealed, with no other airways. Thus, it reduces the electrolyte concentration change and mitigates the formation of carbonate salts, which shortens the lifetime of the battery.

Conclusions

The oxygen selective membranes (OSMs) were fabricated using breath-figures (BF) self-assembly, performed by the dip-coating method from polycarbonate (PC) and oxygen carrier molecules (FePc) on both polypropylene and stainless-steel mesh supports. UV–visible analysis of dissolved membranes was in line with a nominal composition of FePc in the membrane and indicated the interaction between polycarbonate-and FePc. OSMs with various FePc content show limited dependence of oxygen transport properties. Humidity control during membrane fabrication provides an effective

method for reducing water transport, reaching 88% while supporting oxygen limiting current of 73 mA cm^{-2}_{OSM} with an OSM (PC 11%, FePc 9.1%) when applied on the Zn–air cell. GC selectivity results demonstrated facilitated oxygen transport over nitrogen and CO_2, which is applicable for rechargeable Zn–air batteries that are sensitive to the oxygen concentration, CO_2 contamination, and water loss evaporation through the cathode.

Acknowledgements

Compliance with ethical standards

Conflict of interest The authors declare no conflict of interest.

Supplementary Information: The online version of this article (https://doi.org/10.1007/s10853-021-05880-8) contains supplementary material, which is available to authorized users.

References

[1] Blurton KF, Sammells AF (1979) Metal/air batteries: their status and potential—a review. J Power Sources 4:263–279. https://doi.org/10.1016/0378-7753(79)80001-4

[2] Lee JS, Kim ST, Cao R et al (2011) Metal-air batteries with high energy density: Li-air versus Zn-air. Adv Energy Mater 1:34–50. https://doi.org/10.1002/aenm.201000010

[3] Gelman D, Shvartsev B, Ein-Eli Y (2014) Aluminum-air battery based on an ionic liquid electrolyte. J Mater Chem A 2:20237–20242. https://doi.org/10.1039/c4ta04721d

[4] Li CS, Sun Y, Gebert F, Chou SL (2017) Current progress on rechargeable magnesium–air battery. Adv Energy Mater 7:1–11. https://doi.org/10.1002/aenm.201700869

[5] Li Y, Yadegari H, Li X et al (2013) Superior catalytic activity of nitrogen-doped graphene cathodes for high energy capacity sodium–air batteries. Chem Commun 49:11731–11733. https://doi.org/10.1039/C3CC46606J

[6] Kraytsberg A, Ein-Eli Y (2011) Review on Li-air batteries—opportunities, limitations and perspective. J Power Sources 196:886–893. https://doi.org/10.1016/j.jpowsour.2010.09.031

[7] Xu M, Ivey DG, Xie Z, Qu W (2015) Rechargeable Zn-air batteries: progress in electrolyte development and cell configuration advancement. J Power Sources 283:358–371. https://doi.org/10.1016/j.jpowsour.2015.02.114

[8] Wang Q, Lei Y, Chen Z et al (2018) Fe/Fe 3 C@ C nanoparticles encapsulated in N-doped graphene–CNTs framework as an efficient bifunctional oxygen electrocatalyst for robust rechargeable Zn–air batteries. J Mater Chem A 6:516–526

[9] Guo Y, Yuan P, Zhang J et al (2018) Carbon nanosheets containing Discrete Co-N x-B y-C active sites for efficient oxygen electrocatalysis and rechargeable Zn–air batteries. ACS Nano 12:1894–1901

[10] Wei L, Karahan HE, Zhai S et al (2017) Amorphous bimetallic oxide–graphene hybrids as bifunctional oxygen electrocatalysts for rechargeable Zn–air batteries. Adv Mater 29:1701410

[11] Shinde SS, Lee C-H, Sami A et al (2017) Scalable 3-D carbon nitride sponge as an efficient metal-free bifunctional oxygen electrocatalyst for rechargeable Zn–air batteries. ACS Nano 11:347–357

[12] Li B, Geng D, Lee XS et al (2015) Eggplant-derived microporous carbon sheets: towards mass production of efficient bifunctional oxygen electrocatalysts at low cost for rechargeable Zn–air batteries. Chem Commun 51:8841–8844

[13] Lu Q, Guo Y, Mao P et al (2020) Rich atomic interfaces between sub-1 nm RuOx clusters and porous Co3O4 nanosheets boost oxygen electrocatalysis bifunctionality for advanced Zn-air batteries. Energy Storage Mater 32:20–29. https://doi.org/10.1016/j.ensm.2020.06.015

[14] Lu Q, Yu J, Zou X et al (2019) Self-catalyzed rowth of Co, N-Codoped CNTs on carbon-encased CoSx surface: a noble-metal-free bifunctional oxygen electrocatalyst for flexible solid Zn–air batteries. Adv Funct Mater 29:1904481. https://doi.org/10.1002/adfm.201904481

[15] Pan J, Tian XL, Zaman S et al (2019) Recent progress on transition metal oxides as bifunctional catalysts for Lithium-Air and Zinc-Air batteries. Batter Supercaps 2:336–347. https://doi.org/10.1002/batt.201800082

[16] Ismail AF, Khulbe KC, Matsuura T (2015) Gas separation membranes: Polymeric and inorganic

[17] Guo C, Zhou L, Lv J (2013) Effects of expandable graphite and modified ammonium polyphosphate on the flame-retardant and mechanical properties of wood flour-polypropylene composites. Polym Polym Compos 21:449–456. https://doi.org/10.1002/app

[18] Crowther O, Salomon M (2012) Oxygen selective membranes for Li-air (O 2) batteries. Membranes (Basel) 2:216–227. https://doi.org/10.3390/membranes2020216

[19] Robeson LM, Freeman BD, Paul DR, Rowe BW (2009) An empirical correlation of gas permeability and permselectivity in polymers and its theoretical basis. J Memb Sci 341:178–185. https://doi.org/10.1016/j.memsci.2009.06.005

[20] Preethi N, Shinohara H, Nishide H (2006) Reversible oxygen-binding and facilitated oxygen transport in membranes of polyvinylimidazole complexed with cobalt-phthalocyanine. React Funct Polym 66:851–855. https://doi.org/10.1016/j.reactfunctpolym.2005.11.013

[21] Nishide H, Kawakami H, Suzuki T et al (1990) Enhanced stability and facilitation in the oxygen transport through Cobalt Porphyrin Polymer membranes. Macromolecules 23:3714–3716. https://doi.org/10.1021/ma00217a031

[22] Suzuki T, Yasuda H, Nishide H et al (1996) Electrochemical measurement of facilitated oxygen transport through a polymer membrane containing cobaltporphyrin as a fixed carrier. J Memb Sci 112:155–160. https://doi.org/10.1016/0376-7388(95)00291-X

[23] Ghani F, Kristen J, Riegler H (2012) Solubility properties of unsubstituted metal phthalocyanines in different types of solvents. J Chem Eng Data 57(2):439–449. https://doi.org/10.1021/je2010215

[24] Miedema PS, van Schooneveld MM, Bogerd R et al (2011) Oxygen binding to cobalt and iron phthalocyanines as determined from in situ X-ray absorption spectroscopy. J Phys Chem C 115:25422–25428. https://doi.org/10.1021/jp209295f

[25] Baranton S, Coutanceau C, Roux C et al (2005) Oxygen reduction reaction in acid medium at iron phthalocyanine dispersed on high surface area carbon substrate: Tolerance to methanol, stability and kinetics. J Electroanal Chem 577:223–234. https://doi.org/10.1016/j.jelechem.2004.11.034

[26] Lawton EA (1958) The thermal stability of copper phthalocyanine. J Phys Chem 62:384. https://doi.org/10.1021/j150561a051

[27] Bormashenko E, Pogreb R, Stanevsky O et al (2005) Formation of honeycomb patterns in evaporated polymer solutions: influence of the molecular weight. Mater Lett 59:3553–3557. https://doi.org/10.1016/j.matlet.2005.06.026

[28] Nishide H, Tsukahara Y, Tsuchida E (1998) Highly selective oxygen permeation through a Poly(vinylidene dichloride)−cobalt porphyrin membrane: Hopping transport of oxygen via the fixed cobalt porphyrin carrier. J Phys Chem B 102:8766–8770. https://doi.org/10.1021/jp9816317

[29] Bormashenko E, Malkin A, Musin A et al (2008) Mesoscopic patterning in evaporated polymer solutions: Poly(-ethylene glycol) and room-temperature-vulcanized

polyorganosilanes/-siloxanes promote formation of honeycomb structures. Macromol Chem Phys 209:567–576. https://doi.org/10.1002/macp.200700552

[30] Zhou W, Chen J, Li Y et al (2016) Copper mesh templated by breath-figure polymer films as flexible transparent electrodes for organic photovoltaic devices. ACS Appl Mater Interfaces 8:11122–11127. https://doi.org/10.1021/acsami.6b01117

[31] Bormashenko E, Pogreb R, Stanevsky O et al (2005) Mesoscopic and submicroscopic patterning in thin polymer films: Impact of the solvent. Mater Lett 59:2461–2464. https://doi.org/10.1016/j.matlet.2005.03.015

[32] Rodríguez-Hernández J (2020) Breath figures: mechanisms of multi-scale patterning and strategies for fabrication and applications of microstructured functional porous surfaces. Springer, Heidelberg

[33] Billon L, Manguian M, Pellerin V et al (2009) Tailoring highly ordered honeycomb films based on ionomer macromolecules by the bottom-up approach. Macromolecules 42:345–356. https://doi.org/10.1021/ma8020568

[34] Bormashenko E, Balter S, Aurbach D (2012) On the nature of the breath figures self-assembly in evaporated polymer solutions: revisiting physical factors governing the patterning. Macromol Chem Phys 213:1742–1747. https://doi.org/10.1002/macp.201200272

[35] Bormashenko E, Schechter A, Stanevsky O et al (2008) Free-standing, thermostable, micrometer-scale honeycomb polymer films and their properties. Macromol Mater Eng 293:872–877. https://doi.org/10.1002/mame.200800188

[36] Li J, Zhang N, Ni D, Sun K (2011) Preparation of honeycomb porous solid oxide fuel cell cathodes by breath figures method. Int J Hydrogen Energy 36:7641–7648. https://doi.org/10.1016/j.ijhydene.2011.03.118

[37] Bhadra S, Kim NH, Choi JS et al (2010) Hyperbranched poly(benzimidazole-co-benzene) with honeycomb structure as a membrane for high-temperature proton-exchange membrane fuel cells. J Power Sources 195:2470–2477. https://doi.org/10.1016/j.jpowsour.2009.11.083

[38] Stenzel MH, Barner-Kowollik C, Davis TP (2006) Formation of honeycomb-structured, porous films via breath figures with different polymer architectures. J Polym Sci Part A Polym Chem 44:2363–2375. https://doi.org/10.1002/pola.21334

[39] Zou X, Liao K, Wang D et al (2020) Water-proof, electrolyte-nonvolatile, and flexible Li-Air batteries via O2-Permeable silica-aerogel-reinforced polydimethylsiloxane external membranes. Energy Storage Mater 27:297–306. https://doi.org/10.1016/j.ensm.2020.02.014